Experimental Measurement and Compensation of Optical Phase Discontinuities

Thomas E. DeFoor[a], Timothy J. Bukowski[a], Matthew Kalensky[b], and Stanislav Gordeyev[a]

[a]University of Notre Dame, South Bend, Indiana, United States
[b]Naval Surface Warfare Center Dahlgren Division, Dahlgren, Virginia, United States

ABSTRACT

In this paper, we evaluate the effectiveness of adaptive optics (AO) compensation for optical phase discontinuities, akin to the spatial phase functions resulting from laser propagation through a shock wave encountered in free flight. In high subsonic to supersonic flow regimes, shock waves may form local to the beam director of aircraft-mounted laser propagation systems. The discontinuous nature of the spatial phase functions imposed by shock waves may provide challenges in wavefront sensing and hardware correction. To experimentally evaluate the performance of conventional AO solutions, we utilized a benchtop turbulence generator and AO system. Here, we apply simulated phase sheets with optical phase discontinuities to a laser beam using a spatial light modulator; after which, we compensate for them in our AO system using a deformable mirror (DM). In this paper, we demonstrate AO correction informed by both a Digital Holographic wavefront sensor (DHWFS) and a Shack–Hartmann wavefront sensor (SHWFS). Testing of zero-thickness, step-like phase discontinuities shows that the SHWFS is unable to reconstruct the wavefront accurately, leading to poor AO compensation and as a result, no improvement in performance. The DHWFS-based correction, on the other hand, remains reliable and reveals significantly improved AO performance in the presence of phase discontinuities. SHWFS-based AO compensation improves when the phase function is more ramp-like rather than step-like (representing a shock wave of finite thickness); however, problems arise due to discontinuity alignment with DM actuators. The results of this study begin to illustrate the practical challenges of using AO systems to compensate for phase discontinuities.

Keywords: Aero-Optics, Adaptive Optics, Phase Discontinuities, Wavefront Sensing

1. INTRODUCTION

Optical phase discontinuities that arise from abrupt changes in a medium's index of refraction pose significant challenges in the scope of laser-beam propagation. For aircraft-mounted beam propagation systems, these optical phase discontinuities can result from sharp density gradients caused by shock-wave formation at high subsonic and supersonic flight speeds.[1–5] Shock waves represent one type of aero-optical distortion. In general, we can quantify aberrations resulting from aero-optical distortions using the optical path difference (OPD):

$$OPD(x,y) = \int \left[n(x,y,z) - \langle n(x,y,z) \rangle \right] \, dz, \tag{1}$$

where $n(x,y,z)$ is the spatially varying index of refraction and $\langle n(x,y,z) \rangle$ is the spatially averaged index of refraction. OPD is a spatial function representing the equivalent distance in vacuum light must travel in order to achieve the same phase. Variations in the OPD arise from variations in the index of refraction, such as those imposed by turbulent conditions. Through this, the OPD field can be related to the phase field by

$$\phi(x,y) = -\frac{2\pi}{\lambda} \cdot \, OPD(x,y), \tag{2}$$

where λ is the wavelength of the propagating laser light. Variations in $\phi(x,y)$ result in a reduction in system performance in the far field.[2,5,6] For shock waves, the primary focus of this analysis, the optical phase discontinuity often spans the entire measurement aperture. The far-field irradiance implications of beam propagation

Further author information: (Send correspondence to Thomas E. DeFoor)
Thomas E. DeFoor: E-mail: tdefoor@nd.edu

Unconventional Imaging, Sensing, and Adaptive Optics 2025, edited by Jean Dolne, Santasri Bose-Pillai, Matthew Kalensky, Proc. of SPIE Vol. 13619, 136190O · 2025 Published by SPIE
0277-786X · doi: 10.1117/12.3063681

through shock-wave-induced optical phase discontinuities have been numerically and experimentally studied.[7–10] Reference 7 presented analytical relationships between the fluid dynamics of a shock wave and the resulting optical distortions they cause upon propagation. In this work, it was shown that the shock-wave-induced optical phase discontinuity can result in a bifurcation of the far-field irradiance pattern. This behavior was corroborated experimentally in Ref. 8.

Consider the far-field irradiance patterns given in Fig. 1. Presented here is a set of far-field irradiance patterns generated to simulate propagation through optical phase discontinuities of varying strengths. We quantify the strength of the optical phase discontinuity as the change in phase across the discontinuity, $\Delta\phi$. Here, the phase fields are generated to be of "zero thickness" (perfectly discontinuous step function), positioned vertically, and centered horizontally in the aperture. It can be seen that $\Delta\phi$ of sufficient strength causes the irradiance patterns to bifurcate. Additionally, the degree of bifurcation is related to the modulo-2π magnitude of $\Delta\phi$. However, in reality, shock-wave-induced density variations are not completely discontinuous as shock waves do have a finite thickness (on the order of a few μm) and the shock may be at an angle relative to the beam propagation axis. This non-zero thickness can be emulated by replacing the step function in phase with a ramp-like function in phase. More details regarding the modeling of the shock-wave-induced $\Delta\phi$ function are presented in Sec. 2.1.

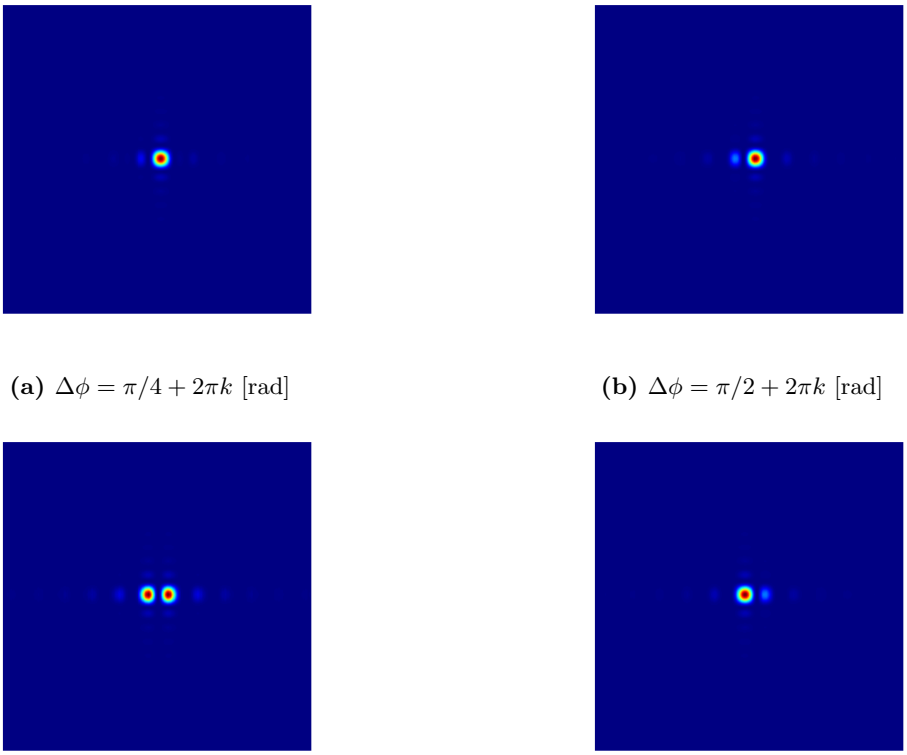

(a) $\Delta\phi = \pi/4 + 2\pi k$ [rad] **(b)** $\Delta\phi = \pi/2 + 2\pi k$ [rad]

(c) $\Delta\phi = \pi + 2\pi k$ [rad] **(d)** $\Delta\phi = 3\pi/2 + 2\pi k$ [rad]

Figure 1: Simulated far-field irradiance patterns disturbed by varying degrees of $\Delta\phi$.

To compensate for optical distortions, adaptive optics (AO) systems are often employed. In practice, AO systems measure phase aberrations using a wavefront sensor; such as a Shack–Hartmann wavefront sensor (SHWFS) or Digital Holographic wavefront sensor (DHWFS). These wavefront sensor measurements inform hardware-based compensation, often using a deformable mirror (DM). Here, the DM applies a conjugate of the measured phase field in order to compensate for the aberrations, as depicted in Fig. 2.

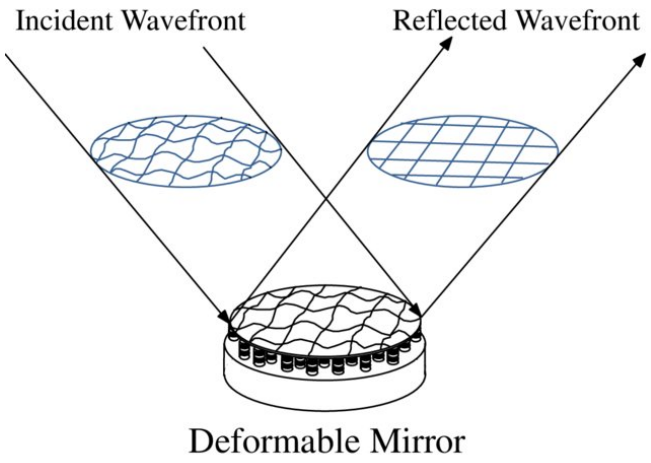

Figure 2: Aberration compensation using a deformable mirror (DM). Figure is from Ref 11.

For the case of optical phase discontinuities, problems begin to arise with both wavefront sensing and DM-based correction. The SHWFS is commonly used for informing AO correction due to its simplicity and robustness. However, the SHWFS, which discretizes the incident wavefront using an array of sub-aperture lenslets, relies on the relationship between local phase tilts in the lenslet pupils manifesting as proportionally shifted irradiance patterns in the image plane. When optical phase discontinuities are present, it has been shown that this relationship breaks down, yielding poor wavefront estimates.[7]

The DHWFS is another wavefront sensing approach which has gained popularity in recent years. The DHWFS is a complex-field sensor and therefore, unlike the SHWFS, does not rely on wavefront slope approximations. With unfettered access to the complex-optical field enabled by DHWFS measurements, we are able to resolve optical phase discontinuities on a modulo-2π basis. Leveraging a phase unwrapping technique, we can then convert the modulo-2π phase field into an "unwrapped" or continuous phase field.

In this study, we experimentally explored the ability of an AO system to compensate for optical phase discontinuities when the correction was informed by both a SHWFS as well as a DHWFS. Our experimental setup is presented in Sec. 2.1. Additionally, information regarding the working principles behind the wavefront sensing techniques is outlined in Sec. 2.2. Our results are presented and discussed in Sec. 3. Section 4 then summarizes the findings of this study.

2. EXPERIMENTAL METHODOLOGY

This section outlines the working principles behind the experimental AO compensation using a continuous sheet DM. First, a description of the experimental turbulence phase generator and AO benchtop setup are provided. The section is then concluded by giving brief overviews of the applied wavefront sensing techniques.

2.1 Experimental Setup

In this study, we utilize a benchtop turbulence generation and AO system to characterize wavefront sensing and DM compensation in repeatable beam propagation scenarios. A simplified schematic of the experimental setup used is presented in Fig. 3. For the purposes of this analysis, we only present the necessary components of the benchtop system; a more detailed description including performance characterization can be found in Refs. 12, 13. The beam coming from the 633 nm, long coherence ($\sim$ 100 m) laser source is split into two main paths; one *reference* path that passes straight from the source to the DHWFS and a *signal* path that is directed to two spatial light modulators (SLMs), the deformable mirror, and then to our SHWFS, DHWFS (where we interfere the signal and reference beam), and through a lens onto the far-field point spread function (PSF) camera for beam profiling. The SLMs impose user-defined phase aberrations onto the signal beam which are consequently measured by the SHWFS and DHWFS. We use the SHWFS and DHWFS measurements to apply

phase conjugation with our DM in closed-loop fashion in order to compensate for the disturbances imposed by the SLMs. The DM was a Boston Micromachines Multi-3.5 MEMS DM with 140 actuators arranged in a 12 x 12 grid spaced 400 μm apart. There were a series of 4f telescopes, which are not pictured, which aligned the conjugate plane of the SLM with the DM and wavefront sensors.

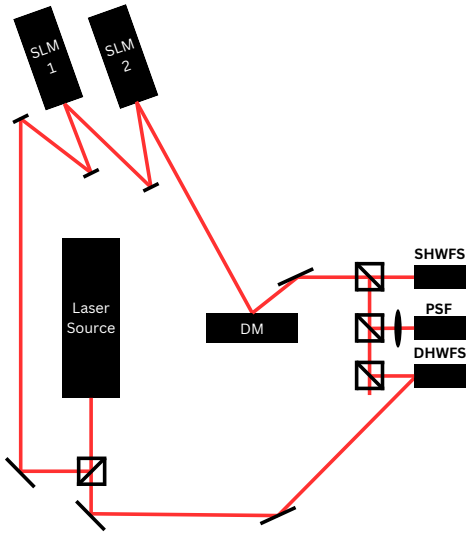

Figure 3: Simplified experimental AO setup (not drawn to scale).

Following the analysis done by Ref. 7, we generate the shock-wave-like phase screens under the assumption that spatial phase function can be represented as a discontinuity. Phase screens were generated for the SLMs of various $\Delta\phi$s from 0 to 2π radians. Additionally, in an attempt to analyze wavefront sensor performance for a broader set of conditions, we also generated the phase screens to include various discontinuity locations, Xs, in the measurement aperture, and widths, w_s. The parameters Xs and w_s are defined in relation to the SHWFS sub-aperture lenslet dimensions (see Fig. 4 for a visual schematic). We define Xs as a fraction of the SHWFS sub-aperture width, w_{ap}, representing a one-dimensional offset from the aperture center. As stated previously, in reality, a shock wave has a small, but non-zero thickness. Additionally, this thickness may be exaggerated by off-axis propagation through a shock wave, as presented in Ref. 7. While not having a significant effect on larger apertures, Xs and w_s are key components when considering the resulting far-field irradiance patterns for SHWFS lenslets. For example, consider Fig. 5. Presented in these figures are simulated PSF and SHWFS images in the presence of a modeled phase discontinuity with $\Delta\phi = \pi$ and $Xs = 0.0$ but with varying w_s values. In Figs. 5a & 5b, $w_s = 0$ and in Figs. 5c & 5d, $w_s = \frac{w_{ap}}{3}$. To reiterate, this means that the phase is represented by a ramp function with a width $\frac{w_{ap}}{3}$ and height π, located in the center of a column of SHWFS sub-apertures, as visible in Fig. 5c. It is clear to see here that there is no discernible difference between the PSF images in Fig. 5b and Fig. 5d while there is a noticeable difference between the SHWFS images in Fig. 5a and Fig. 5c, where there is additional spreading of the resulting SHWFS irradiance patterns due to a nonzero w_s.

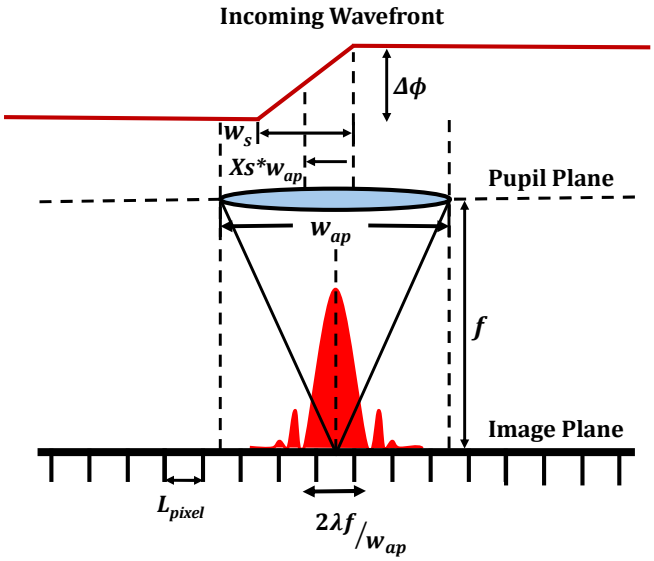

Figure 4: Visual representation of phase function parameters.

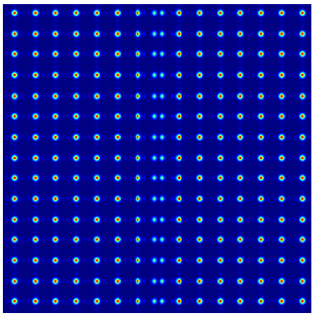

(a) SHWFS, $w_s = 0$

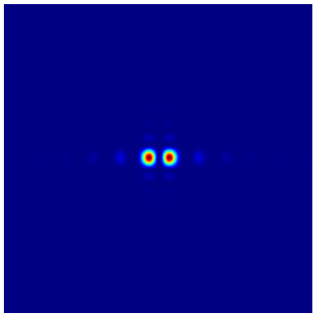

(b) PSF, $w_s = 0$

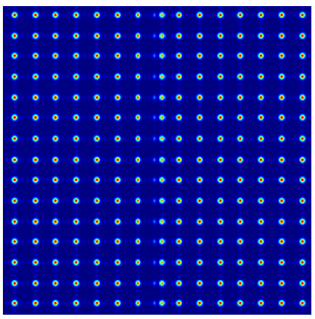

(c) SHWFS, $w_s = \frac{w_{ap}}{3}$

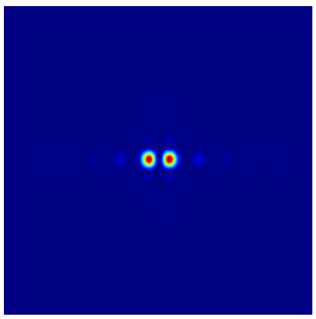

(d) PSF, $w_s = \frac{w_{ap}}{3}$

Figure 5: Simulated Shack–Hartmann Wavefront Sensor (SHWFS) and Point Spread Function (PSF) data for $\Delta\phi = \pi$, Xs $= 0$, and $w_s = 0$ (a – b), $\frac{w_{ap}}{3}$ (c – d)

2.2 Wavefront Reconstruction

In this study, we also analyze the effectiveness of the SHWFS and DHWFS methods in informing AO correction via a DM. The SHWFS consists of an array of sub-aperture lenslets that focus portions of the incident light into individual spots on a detector screen. When there is a tilt present in the incident phase local to a lenslet, the individual irradiance pattern shifts from its on-axis position. This centroid shift, d, is measured and used along with the lenslet focal length, f, to estimate the local phase tilt, $\theta = d/f$, which is then fed into a least squares reconstructor to estimate the wavefront across the SHWFS aperture.[14–16] The specific SHWFS used in this study is the ThorLabs WFS20-5C. The SHWFS was configured such that the measurement area was 5.4 mm × 5.4 mm, allowing for wavefront reconstruction using 32×32 sub-apertures, each with a pitch of 150 μm. An example experimentally collected SHWFS image and resulting least squares reconstructed phase is shown in Fig. 6 for the case of $\Delta\phi = \pi$ radians located in the center of the aperture. In Fig. 6a, a line of bifurcated sub-aperture irradiance patterns is visible which correspond to the location of the shock wave. However, the least squares reconstructed phase shown in Fig. 6b is flat. This is due to the fact that in this case, the optical phase discontinuity results in the measured centroid shifts not proportionally mapping to the local lenslet phase, leading to the inaccurate wavefront reconstruction shown in Fig. 6b.

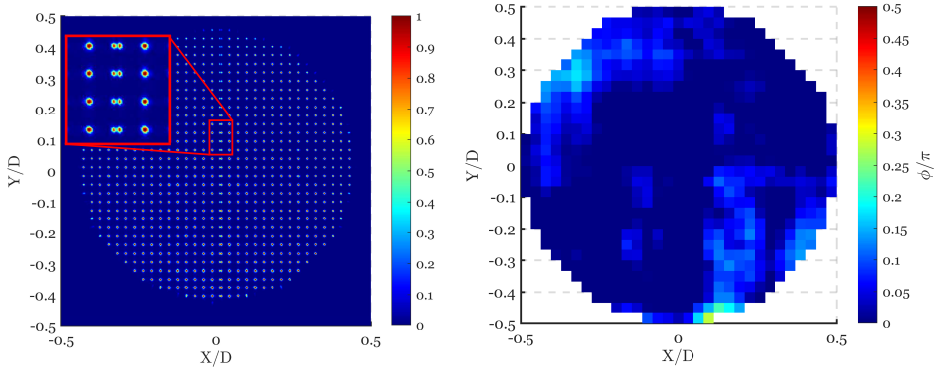

(a) SHWFS Image **(b)** Least Squares Reconstructed Phase

Figure 6: Example Shack–Hartmann Wavefront Sensor data in the the presence of a shock-wave-like $\Delta\phi = \pi$ oriented vertically and located in the center of the measurement aperture.

Conversely, the DHWFS provides higher spatial resolution through which larger phase gradient magnitudes are able to be resolved.[17–19] The DHWFS utilizes the interference between two coherent beams, one reference which passes from the source to the detector, and one signal that passes through the aberration of interest then to the detector. The detector used here was a Mikrotron EoSens 3.0MCL-CM CMOS camera with a resolution of 3 MP, with an individual pixel size of 8×8 μm. In this study, we use the off-axis pupil plane recording geometry, where the collimated signal and reference beams interfere at an angle. This implementation of digital holography has been studied thoroughly in the literature.[18,20–22] Using the off-axis geometry, the tilt angle determines the spatial frequency of the resulting interference fringes. In this experiment, the processed complex-optical field obtained from our DHWFS measurements had a resolution of 41×41 pixels. A downsampled resolution was chosen to allow for a faster AO loop rate. The phase function of the complex-optical field extracted from our DHWFS measurements is "wrapped" (i.e., confined to a modulo-2π radian range) and requires phase unwrapping techniques to reconstruct a continuous wavefront estimate. Similar to the SHWFS, it is common to use a least-squares reconstructor to estimate the unwrapped phase. For example, refer to Fig. 7. Plotted in Fig. 7a is the wrapped phase extracted from the complex-optical field of our DHWFS measurement for the case of $\Delta\phi = \pi$ radians, Xs = 0, and $w_s = 0$. After least squares reconstruction (and removal of an additive global tip/tilt), a continuous phase field is gained, as plotted in Fig. 7b.

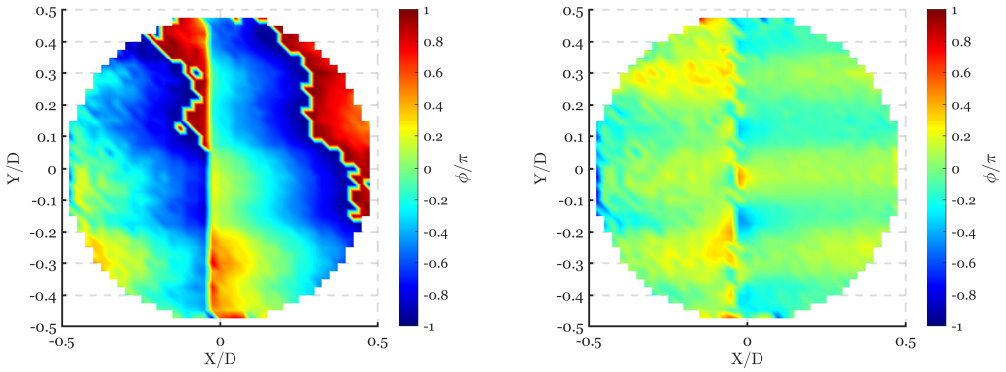

(a) Wrapped Phase **(b)** Unwrapped Phase

Figure 7: Example phase functions processed using DHWFS measurements in the the presence of a optical phase discontinuity where $\Delta\phi = \pi$, Xs = 0, and $w_s = 0$.

3. RESULTS

This section presents the results of closed-loop AO compensation informed by both our SHWFS and DHWFS. To reiterate, phase fields were generated to replicate optical phase discontinuities. For the tests conducted here, we generated optical discontinuities where $\Delta\phi = 0 - 2\pi$ radians, $Xs = 0.0$ & 0.4, and $w_s = 0$, $\frac{w_{ap}}{3}$, & $\frac{2w_{ap}}{3}$. To quantify the performance of our AO compensation, we utilized the normalized power in the bucket, nPIB, metric. We compute the discretized power in the bucket as

$$PIB = \sum_{x,y \leq D_b} = I(x,y)\Delta x \Delta y, \tag{3}$$

where D_b is the bucket diameter and I(x, y) is the irradiance at the detector plane. The bucket diameter was defined as twice the radial distance from the beam centroid at which the normalized intensity falls to e^{-2} of its peak value, i.e., $\frac{I}{I_{max}} = e^{-2}$. This bucket diameter was calculated for the non-aberrated case and held constant for all test cases. We normalized PIB calculated during AO compensation by the PIB we obtained when no phase aberrations were present on the SLMs. The results of this testing are presented in Fig. 8. Here, the x axis is the input $\Delta\phi/\pi$ and the y axis is PIB_n. Our time-averaged AO on results using the DHWFS are depicted using blue circles, our time-averaged AO on results using the SHWFS are depicted using red asterisks, and our time-averaged AO off results are depicted using black crosses. Each subplot represents a different Xs and w_s condition.

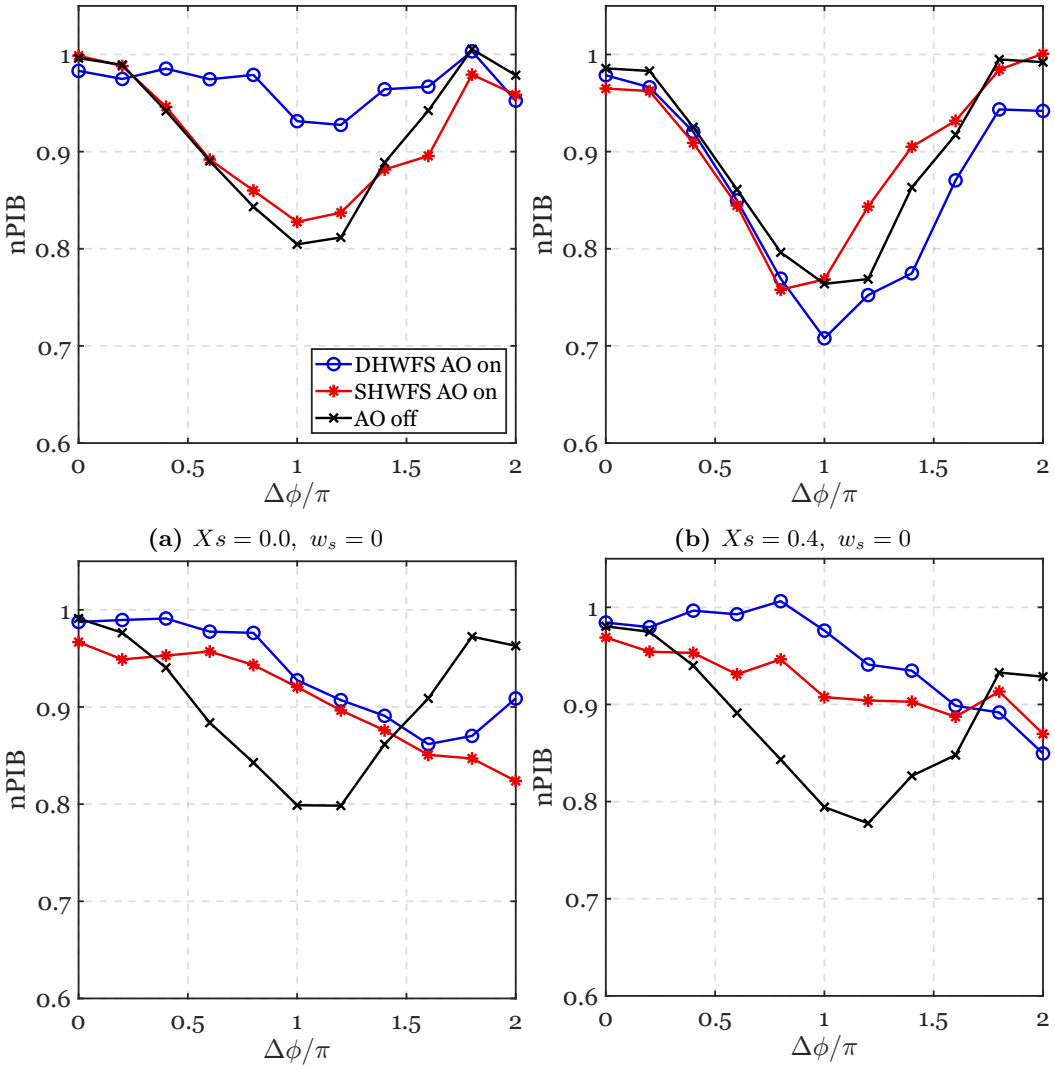

(a) $Xs = 0.0,\ w_s = 0$ **(b)** $Xs = 0.4,\ w_s = 0$

(c) $Xs = 0.0,\ w_s = \frac{w_{ap}}{3}$ **(d)** $Xs = 0.0,\ w_s = \frac{2w_{ap}}{3}$

Figure 8: Normalized PIB vs. $\Delta\phi/\pi$ for various Xs & w_s

Figure 8a presents the results for the case of Xs=0 and $w_s = 0$. There is a "u-shape" in nPIB results for the AO off case due to how the degree of bifurcation varies with $\Delta\phi$; where no bifurcation occurs at $\Delta\phi = 0,\ 2\pi$ radians and the most bifurcation occurs at $\Delta\phi = \pi$ radians. Focusing on the DHWFS curve, there is clear improvement when AO is turned on across all $\Delta\phi$ values, where the nPIB does not drop below ~0.92, showing that DHWFS accurately measures the incident phase and the DM is capable of applying the correct phase conjugation. On the other hand, we see that the SHWFS offers no improvement when AO compensation is applied. The failure of the SHWFS in this case can be attributed to the non-proportionality between the measured centroid offset and the incident phase at the pupil plane of the sensor, leading to incorrect measurements. Single PSF frames for AO on and AO off for the case of $\Delta\phi = \pi$ for both SHWFS and DHWFS are presented in Fig. 9. Here it is clear that we see significant improvement in performance when using the DHWFS to inform AO compensation (Fig. 9a and 9b), while we see the focused irradiance pattern is mostly unchanged with the SHWFS (Fig. 9c and 9d).

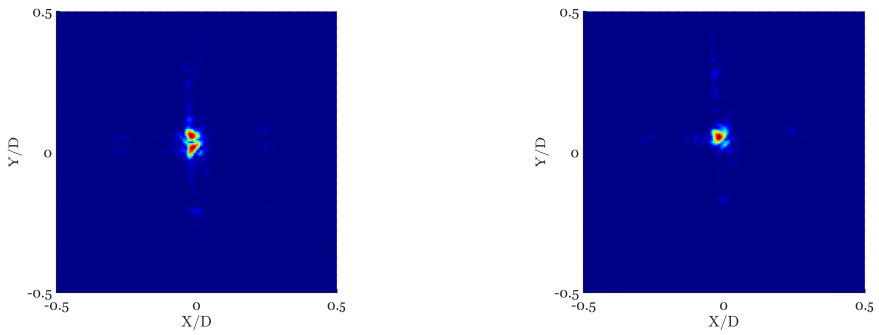

(a) DHWFS, AO off **(b)** DHWFS, AO on

(c) SHWFS, AO off **(d)** SHWFS, AO on

Figure 9: Single frames taken for AO off and AO on for the DHWFS and SHWFS for the case of $\Delta\phi = \pi$ radians, Xs = 0, $w_s = 0$

Figure 8b presents our results for the case where Xs=0.4 and $w_s = 0$. This corresponds to the discontinuity being offset by 40% of a SHWFS sub-aperture width away from center. Similar to Fig. 8a, the u-shape in the AO off performance results is due to the relationship between degree of bifurcation and $\Delta\phi$. However, we see that the DHWFS-based AO compensation no longer improves performance and closely follows the AO off and SHWFS results. This degradation in performance can be attributed to the location of the optical phase discontinuity relative to the column of DM actuators. An offset of Xs = 0.4 corresponds to a spatial offset of roughly 160 μm on the DM, which is also nearly half the inter-actuator pitch. By this reasoning, we deduce that when Xs = 0, the optical phase discontinuity was located between two actuators, allowing for the DM to recreate the step-like function in phase. However, shifting by Xs = 0.4 or half of an actuator pitch (Fig. 8b) places the optical phase discontinuity location at or near the center of an actuator, which prohibits the DM from replicating the step-like phase function. Future iterations of these experiments will explore this effect in greater detail.

Figures 8c & 8d present nPIB results for the cases of Xs = 0 with $w_s = w_{ap}/3,\ 2w_{ap}/3$, respectively. To reiterate,$w_s = w_{ap}/3,\ 2w_{ap}/3$ correspond to ramp widths at 1/3 and 2/3 of the SHWFS sub-aperture width. Here we see that the SHWFS- and DHWFS-based AO results now yield similar nPIB performance across all $\Delta\phi$. We see comparable performance to the AO off case when $\Delta\phi$ is small. This is because the optical phase discontinuity is weak and therefore, AO is not needed in order to achieve good performance. We indeed see a substantial increase in performance using both the SHWFS as well as the DHWFS to inform our AO correction for $\Delta\phi \approx 0.5 - 1.5$ radians. This is due to the fact that the optical phase function is more akin to a local tilt with respect to the SHWFS sub-aperture width which will result in a shifted irradiance pattern rather than a bifurcated irradiance pattern, as illustrated earlier in Figs. 5a & 5c. However, both the DHWFS and SHWFS AO on cases decrease in nPIB as $\Delta\phi$ increases, ultimately yielding worse performance than our AO off case. Unfortunately, there is not enough data at the current state of this analysis to fully diagnose and explain these results. However, a few testable hypotheses exist. One of which attributes error to DM phase conjugation where values of $w_s = w_{ap}/3,\ 2w_{ap}/3$ correspond to spatial widths of 50 and 150 μm on the DM, respectively, which is

less than the inter-actuator pitch. As these cases were located in the same position on the DM as the results presented in Fig. 8a, these phase functions are placed at the interface between two actuators, causing the ramp function to be represented by only two actuators. Therefore, the resulting phase from DM actuation resembles a step function rather than the ramp, leading to inaccurate phase conjugation. Future iterations will include a deeper analysis and trade study sweep to fully resolve the issues associated with optical phase compensation using a continuous sheet deformable mirror.

4. CONCLUSIONS

In this paper, we experimentally examined the performance of an AO system in correcting for optical phase discontinuities, such as the ones resulting from propagation through shock waves. To evaluate the performance of AO compensation in the presence of such optical phase discontinuities, we utilized a benchtop turbulence generation and AO system. Specifically, we used SLMs to impose user-defined optical phase discontinuities onto the beam. We then used our AO system to correct for the optical phase discontinuities. Here, we used both a SHWFS as well as a DHWFS to inform our correction. We evaluated performance with a PSF camera and quantified performance using nPIB.

We showed that the DHWFS accurately informs AO correction in the presence of zero-thickness, optical phase discontinuities ranging from $\Delta\phi = 0 - 2\pi$ radians. The SHWFS, however, was unable to inform AO compensation due to the non-proportionality between measured sub-aperture irradiance pattern shifts and incident pupil phase caused by the far-field bifurcation. We also found that AO performance can degrade depending on the location of the optical phase discontinuities relative to the DM actuators. Specifically, when the optical phase discontinuity was located between DM actuators, we found that the DM was able to compensate for the optical phase discontinuity. On the other hand, when the optical phase discontinuity was located directly on top of the DM actuators, the DM was unable to correct for it.

It was also found that when the optical phase discontinuity function was modeled as a ramp of predefined thickness, the SHWFS algorithm performed similarly to the DHWFS. By increasing the width of the phase discontinuity function, the resulting sub-aperture irradiance pattern centroid shift became more indicative of the pupil phase, leading to accurate reconstruction of the wavefront. However, at the higher end of $\Delta\phi$ values, undiagnosed appreciable error was introduced that is hypothesized to be attributed to DM hardware error in physically modeling the phase function. Future iterations of this study will aim to resolve such issues left unanswered by the current analysis by expanding the trade space to more rigorously test DM-based AO correction in the presence of optical phase discontinuities. Largely, this research informs efforts looking to conduct AO in aero-optical environments.

Funding Sources

Grateful acknowledgment is given to the Joint Directed Energy Transition Office (JDETO), whose sponsorship of Notre Dame's Aero Optics Group and Government Owned Adaptive-optics Technologies + (GOAT+) project has made this work possible.

Disclosures

The U.S. Government is authorized to reproduce and distribute reprints for governmental purposes notwithstanding any copyright notation thereon.

Distribution Statement A. Approved for public release: distribution is unlimited.

REFERENCES

[1] Gilbert, K. G. and Otten, L. J., [*Aero-Optical Phenomena*], American Institute of Aeronautics and Astronautics, New York (1982). _eprint: https://arc.aiaa.org/doi/pdf/10.2514/4.865541.

[2] Gordeyev, S., Jumper, E., and Whiteley, M., [*Aero-optical effects: Physics, Analysis and Mitigation*], John Wiley & Sons (2023).

[3] Jumper, E. J. and Gordeyev, S., "Physics and measurement of aero-optical effects: past and present," *Annual Review of Fluid Mechanics* **49**(1), 419–441 (2017).

[4] Kalensky, M., Gordeyev, S., Kemnetz, M. R., and Spencer, M. F., "Aero-optical effects, part I. system-level considerations: tutorial," *JOSA A* **41**, 2163–2174 (Nov. 2024). Publisher: Optica Publishing Group.

[5] Kalensky, M., Gordeyev, S., Kemnetz, M. R., and Spencer, M. F., "Aero-optical effects, part II. Sources of aberrations: tutorial," *JOSA A* **41**, 2175–2187 (Nov. 2024). Publisher: Optica Publishing Group.

[6] Kalensky, M., Wells, J., and Gordeyev, S., "Image degradation due to different in-flight aero-optical environments," *Optical Engineering* **59** (Oct. 2020).

[7] Kalensky, M., Kemnetz, M. R., and Spencer, M. F., "Effects of shock waves on shack–hartmann wavefront sensor data," *AIAA Journal* , 1–13 (mar 2023).

[8] Kemnetz, M. R., Kalensky, M., DeFoor, T. E., and Spencer, M. F., "Experimental investigation into the effects of shock waves on Shack-Hartmann wavefront sensor measurements," in [*Unconventional Imaging, Sensing, and Adaptive Optics 2023*], **12693**, 353–364, SPIE (Oct. 2023).

[9] DeFoor, T. E., Kalensky, M., Kemnetz, M. R., Bukowski, T. J., and Spencer, M. F., "Shock-wave tolerant phase reconstructor for the Shack–Hartmann wavefront sensor," in [*Unconventional Imaging, Sensing, and Adaptive Optics 2023*], **12693**, 228–236, SPIE (Oct. 2023).

[10] DeFoor, T. E., Bukowski, T. J., Kalensky, M., and Gordeyev, S., "Phase discontinuity classification from single-aperture irradiance patterns using machine learning," in [*Unconventional Imaging, Sensing, and Adaptive Optics 2024*], **13149**, 156–167, SPIE (Oct. 2024).

[11] Steinbock, M., "Implementation of Branch-Point-Tolerant Wavefront Reconstructor for Strong Turbulence Compensation," (June 2012).

[12] Bukowski, T. J., Kalensky, M., Getts, D., and Gordeyev, S., "Comparison of Shack–Hartmann and digital holographic wavefront sensing using a benchtop turbulence generator," in [*Unconventional Imaging, Sensing, and Adaptive Optics 2024*], Kalensky, M., Dolne, J. J., and Bose-Pillai, S. R., eds., **1314910**, International Society for Optics and Photonics, SPIE (2024).

[13] Kalensky, M., Getts, D., Bukowski, T. J., Rowe, M., Hui, N., and Clifford, Y., "Benchtop adaptive-optics testing in the presence of scintillation," *Journal of Optics* (2025).

[14] Fried, D. L., "Least-square fitting a wave-front distortion estimate to an array of phase-difference measurements," *JOSA* **67**, 370–375 (Mar. 1977). Publisher: Optica Publishing Group.

[15] Hudgin, R. H., "Wave-front reconstruction for compensated imaging," *JOSA* **67**, 375–378 (Mar. 1977). Publisher: Optica Publishing Group.

[16] Southwell, W. H., "Wave-front estimation from wave-front slope measurements," *JOSA* **70**, 998–1006 (Aug. 1980). Publisher: Optica Publishing Group.

[17] Wilcox, C. C., Radosevich, C. J., Healy, K. P., Tuffli, A. L., Agena, B. D., and Mark F. Spencer, D. J. W. I., "Digital holography wavefront sensing with a super wind tunnel," **11030**, SPIE (April 2019).

[18] Spencer, M. F., "Spatial heterodyne," in [*Encyclopedia of Modern Optics (Second Edition)*], Guenther, B. D. and Steel, D. G., eds., 369–400, Elsevier, Oxford, second edition ed. (2018).

[19] Chu, E. D., Bukowski, T. J., and Gordeyev, S., "Improved wavefront reconstruction for shack–hartmann wavefront sensor in the presence of shock-related distortions," *Optics and Laser Technology* **187**, 112764 (2025).

[20] Banet, M. T., Spencer, M. F., and Raynor, R. A., "Digital-holographic detection in the off-axis pupil plane recording geometry for deep-turbulence wavefront sensing," *Applied Optics* **57**, 465 (jan 2018).

[21] Banet, M. T., Spencer, M. F., Raynor, R. A., and Marker, D. K., "Digital holography wavefront sensing in the pupil-plane recording geometry for distributed-volume atmospheric aberrations," in [*SPIE Proceedings*], Dolne, J. J., Karr, T. J., and Dayton, D. C., eds., SPIE (sep 2016).

[22] Banet, M. T. and Spencer, M. F., "Multiplexed digital holography for simultaneous imaging and wavefront sensing," in [*Unconventional and Indirect Imaging, Image Reconstruction, and Wavefront Sensing 2019*], Dolne, J. J., Spencer, M. F., and Testorf, M. E., eds., **11135**, 1113503, International Society for Optics and Photonics, SPIE (2019).